

Large-Scale Simulation Unveiled Superior Potassium-Based Solid Electrolyte with High Ionic Conductivity and Excellent Electrochemical Stability in $M_5\text{YSi}_4\text{O}_{12}$ ($M = \text{Li}, \text{K}$)

Zhao Li,^{1,*} Jiaxiang Li,^{1,*} Congwei Xie,^{2,†} Keith Butler,³ Fei Du,⁴ and Yu Xie^{1,4,‡}

¹Key Laboratory of Material Simulation Methods and Software of Ministry of Education, College of Physics, Jilin University, Changchun 130012, China

²Research Center for Crystal Materials, State Key Laboratory of Functional Materials and Devices for Special Environmental Conditions, Xinjiang Key Laboratory of Functional Crystal Materials, Xinjiang Technical Institute of Physics and Chemistry, Chinese Academy of Sciences, 40-1 South Beijing Road, Urumqi 830011, China

³Department of Chemistry, University College London, Gordon Street, London WC1H 0AJ, United Kingdom

⁴Key Laboratory of Physics and Technology for Advanced Batteries of Ministry of Education, College of Physics, Jilin University, Changchun 130012, China



(Received 15 January 2025; revised 29 June 2025; accepted 8 July 2025; published 14 August 2025)

Simultaneously achieving interfacial stability and high room-temperature ionic conductivity ($\geq 10^{-3}$ S/cm) in solid-state electrolytes is one of the most significant challenges in the development of all-solid-state batteries. In this study, by combining first-principles simulations and large-scale machine-learning molecular dynamics modeling, we demonstrate $K_5\text{YSi}_4\text{O}_{12}$ is such an outstanding electrolyte for K-ion batteries that showcases both intrinsic interfacial stability with metal anode and fast ion diffusivity. Conversely, $\text{Li}_5\text{YSi}_4\text{O}_{12}$ only exhibits mediocre performance for Li-ion batteries. Our results show $\text{Li}_5\text{YSi}_4\text{O}_{12}$ is thermodynamically unstable and will be reduced by the metal anode, whereas thermodynamically stable $K_5\text{YSi}_4\text{O}_{12}$ presents a wide electrochemical stability window of 0.00–3.27 V *versus* K/K⁺, suggesting it is stable in contact with potassium metal. The predicted ionic conductivity is 0.43 and 3.63 mS/cm for $\text{Li}_5\text{YSi}_4\text{O}_{12}$ and $K_5\text{YSi}_4\text{O}_{12}$, respectively. Moreover, a significant size effect has been observed in $K_5\text{YSi}_4\text{O}_{12}$, where the accurate ionic conductivity can only be obtained through large-scale simulations. Further analysis reveals low energy barrier and long hopping distance are responsible for the higher ionic conductivity in $K_5\text{YSi}_4\text{O}_{12}$. This work identifies an excellent electrolyte candidate for K-ion batteries and underscores the importance of scale in the modeling of ionic conductivity.

DOI: 10.1103/8wkh-238p

I. INTRODUCTION

Solid-state electrolytes (SSEs) that enable the use of metal anodes by replacing the flammable liquid electrolytes are a key component of the next-generation high-safety and high-energy-density all-solid-state batteries (ASSBs) [1–4]. The ideal SSEs should excel simultaneously in all the desired properties, including high room-temperature ionic conductivity, good electrochemical stability, high compressibility, and low cost [5,6].

However, most of the studied SSEs either exhibit high room-temperature ionic conductivity ($> 10^{-3}$ S/cm) but are unstable against the metal anode (e.g., sulfides) or present excellent stability with the electrodes but the ionic conductivity is limited (e.g., oxides), preventing the large-scale commercialization of ASSBs. Thus, it is an emergent challenge to discover SSEs with both high ionic conductivity and intrinsically stable electrode-electrolyte interfaces.

$\text{Na}_5X\text{Si}_4\text{O}_{12}$ ($X = \text{Fe}, \text{In}, \text{Sc}, \text{Y}$, and the rare earth Lu-Sm) N5-type compounds, known for their high ionic conductivities with open channels in the structural framework [7–10], have recently attracted notable attention in the field of ASSBs [11–17]. The first systematic study of these materials was conducted by Shannon *et al.* [7] four decades ago, revealing that the ionic conductivities increased with the ionic radius of the X-site element and could reach 10^{-1} S/cm at 200 °C. Subsequent research by Beyeler *et al.* [8] investigated the ionic conductivity along different crystallographic directions in a single crystal of $\text{Na}_5\text{YSi}_4\text{O}_{12}$.

*These authors contributed equally to this work.

†Contact author: cxwxe@ms.xjb.ac.cn

‡Contact author: xieyu@jlu.edu.cn

Room-temperature conductivities parallel and perpendicular to the hexagonal *c*-axis were determined to be 3.2 and 8 mS/cm. More recently, Sun *et al.* [18] synthesized $\text{Na}_5\text{YSi}_4\text{O}_{12}$ and assembled it into ASSBs, achieving an ionic conductivity of 1.59 mS/cm at room temperature and demonstrating electrochemical stability up to 8 V, comparable to well-known SSEs such as $\text{Na}_3\text{Zr}_2\text{Si}_2\text{PO}_{12}$ and Na_3PS_4 , both of which exhibit stability above 5 V in experiments [19,20]. Further studies by Lou *et al.* [21] confirmed fast ionic mobility in $\text{Na}_5\text{YSi}_4\text{O}_{12}$ along open channels and substantial diffusion between them.

The large void space, fast Na^+ mobility, and wide electrochemical window of the N5-type structure suggest it might also be good ionic conductor for Li^+ and K^+ , serving as potential SSEs for Li-ion and K-ion batteries. K-ion batteries have emerged as promising alternatives to Li-ion batteries due to their economic viability (K crustal abundance of 2.09 wt% versus Li at 0.0017 wt%) and comparable electrochemical performance. The K^+/K redox potential (-2.93 V vs. SHE) approaches that of Li^+/Li (-3.04 V) while being lower than Na^+/Na (-2.71 V), suggesting high-energy-density potential for K-ion batteries [22–25]. Notably, the substitution strategy has already been successfully applied in the development of promising SSEs for all sorts of solid-state batteries. [26,27]. For instance, Li-NASICON and K_3SbS_4 SSEs are derived from Na-NASICON and Na_3PS_4 SSEs, respectively [28–30]. $\text{Na}_{10}\text{SnP}_2\text{S}_{12}$ is developed through elemental substitution from $\text{Li}_{10}\text{GeP}_2\text{S}_{12}$ [31]. The Li-argyrodite SSEs trace their origins to the silver superionic conductor Ag_8GeS_6 [32]. Moreover, Shannon *et al.* [7] tried to substitute Na^+ with Li^+ and K^+ for $\text{Na}_5\text{YSi}_4\text{O}_{12}$ in their pioneering work. They successfully synthesized $\text{Li}_5\text{YSi}_4\text{O}_{12}$ with molten salt exchange method using molten LiNO_3 at 350°C . However, the ionic conductivity was not measured, probably due to mixed compositions. They also attempted to synthesize $\text{K}_5\text{YSi}_4\text{O}_{12}$ using molten KNO_3 but were unsuccessful, possibly due to the larger ion radius of potassium that makes the molten salt exchange method unsuitable. Therefore, the feasibility of Li- and K-substituted $\text{Na}_5\text{YSi}_4\text{O}_{12}$ as SSEs remains an open question, which prompts us to explore whether $\text{Li}_5\text{YSi}_4\text{O}_{12}$ and $\text{K}_5\text{YSi}_4\text{O}_{12}$ can achieve high stability and high ionic conductivity simultaneously.

In this study, we investigate the potential of $\text{Li}_5\text{YSi}_4\text{O}_{12}$ and $\text{K}_5\text{YSi}_4\text{O}_{12}$ as SSEs by examining their stability and ionic conductivity through theoretical simulations. To provide comprehensive comparison and to complement existing experimental studies, similar investigations are also performed for $\text{Na}_5\text{YSi}_4\text{O}_{12}$. Our calculations confirm that both $\text{Li}_5\text{YSi}_4\text{O}_{12}$ and $\text{K}_5\text{YSi}_4\text{O}_{12}$ are insulators with wide band gaps. While $\text{Li}_5\text{YSi}_4\text{O}_{12}$ is found to be thermodynamically unstable, $\text{K}_5\text{YSi}_4\text{O}_{12}$ demonstrates thermodynamic stability. Notably, $\text{K}_5\text{YSi}_4\text{O}_{12}$ exhibits intrinsic stability when in contact with potassium metal anode. The

ionic conductivity and diffusion patterns of $M_5\text{YSi}_4\text{O}_{12}$ ($M = \text{Li}, \text{Na}, \text{K}$) are analyzed using a combination of first-principles and machine-learning-accelerated molecular dynamics. Within the $M_5\text{YSi}_4\text{O}_{12}$ structural framework, lithium ions exhibit diffusion both along the open channels and within planes perpendicular to these channels, whereas potassium ions primarily diffuse along the open channels. Machine-learning-accelerated molecular dynamics reveals that $\text{Na}_5\text{YSi}_4\text{O}_{12}$ can achieve a room-temperature ionic conductivity of 6.11 mS/cm, followed by $\text{K}_5\text{YSi}_4\text{O}_{12}$ (3.63 mS/cm) and $\text{Li}_5\text{YSi}_4\text{O}_{12}$ (0.43 mS/cm). Interestingly, a significant size effect is observed in $\text{K}_5\text{YSi}_4\text{O}_{12}$, where accurate estimates of ionic conductivity require large simulation supercells. Our findings confirm $\text{K}_5\text{YSi}_4\text{O}_{12}$ as a promising candidate for potassium-based SSEs, whereas $\text{Li}_5\text{YSi}_4\text{O}_{12}$ is less suitable due to its instability and low ionic conductivity.

II. COMPUTATIONAL METHODS

A. Structure constructing

The crystal structure of $\text{Na}_5\text{YSi}_4\text{O}_{12}$ is obtained from the Inorganic Crystal Structure Database (ICSD) with collection code 20272. The structure crystallizes in the space group $R\bar{3}c$ (No. 167) containing 396 atoms per cell, where sodium sites exhibit fractional occupancies. Detailed atomic coordinates are listed in Table S1 in the Supplemental Material [33]. $\text{Na}_5\text{YSi}_4\text{O}_{12}$ belongs to the trigonal crystal system, which can be represented in either hexagonal (as indicated by Table S1) or rhombohedral settings (as indicated by Table S2). The rhombohedral setting corresponds to its primitive cell, containing 132 atoms. In this work, we develop a specially designed primitive cell for molecular dynamics simulations using the approach implemented in PYMATGEN [34], which preserves both the atomic count and volume of the rhombohedral cell while enabling clearer visualization of ion diffusion pathways. The lattice parameters of this modified primitive cell are provided in Table S3. In Sec. I.A of the Supplemental Material [33] (see also references [35–43] therein), we thoroughly describe the transformation matrices between the special primitive cell and the rhombohedral primitive cell.

The fractional occupancy of Na^+ sites in the primitive cell are dealt by systematic enumeration of all possible sodium ion configurations, yielding a total of 735 471 candidate structures. These configurations are sorted by their electrostatic energy with PYMATGEN [34]. The 20 configurations with the lowest electrostatic energies are selected for subsequent first-principles structural relaxation. The lowest-energy configuration is selected for further analysis. For lithium and potassium ion systems, the same enumeration and optimization procedures are performed based on elemental substitution in the sodium ion primitive cell. Figure S2 of the Supplemental Material [33]

TABLE I. Comparison of the energy above the convex hull (E_{hull} , meV/atom), ionic radius of M ions (R_{M+} , Å), lattice parameters (Å), and volume of the primitive cell (Å³) for $M_5\text{YSi}_4\text{O}_{12}$ ($M = \text{Li}, \text{Na}, \text{K}$). The ionic radii are based on the values reported by Shannon [44].

Compound	E_{hull}	R_{M+}	a	b	c	V	$V_{M_5\text{YSi}_4\text{O}_{12}}/V_{\text{Na}_5\text{YSi}_4\text{O}_{12}}$
$\text{Li}_5\text{YSi}_4\text{O}_{12}$	40	0.59	12.11	12.82	13.04	1589.27	87%
$\text{Na}_5\text{YSi}_4\text{O}_{12}$	0	0.99	12.75	13.52	13.56	1825.41	100%
$\text{K}_5\text{YSi}_4\text{O}_{12}$	0	1.37	13.66	14.08	14.08	2099.49	115%

presents the energy distribution of optimized $M_5\text{YSi}_4\text{O}_{12}$ configurations, where the 20 lowest-electrostatic-energy configurations exhibit a concentrated energy distribution after structural optimization, indicating minimal energy differences between distinct configurations. The refined structural parameters are summarized in Table I. Details of optimized structure are presented in Tables S4 and S5 of the Supplemental Material [33]. Notably, while the Perdew-Burke-Ernzerhof (PBE) functional systematically overestimates lattice constants in most cases, we observe remarkably small deviations of only 0.5%, 0.5%, and 0.8% along the a -, b -, and c -axes for $\text{Na}_5\text{YSi}_4\text{O}_{12}$ when comparing our calculations with the primitive cell derived from experimental data (Table S3). This minimal discrepancy demonstrates that the PBE-induced lattice expansion has a negligible effect on our conclusions regarding ion transport properties.

B. DFT calculations

All density functional theory (DFT) calculations are performed using the Vienna Ab initio Simulation Package (VASP) [45]. A plane-wave cutoff of 520 eV and a \mathbf{k} -point grid density of $3 \times 3 \times 3$ are used for DFT relaxations and energy calculations, consistent with the settings used in the Materials Project database [46]. The phase stability of $M_5\text{YSi}_4\text{O}_{12}$ ($M = \text{Li}, \text{K}$) is assessed by calculating their energy above convex hull (E_{hull}) in the respective $M\text{-Y-Si-O}$ ($M = \text{Li}, \text{K}$) phase diagrams. Compounds with $E_{\text{hull}} = 0$ eV are thermodynamically stable, while higher values indicate increasing instability. For constructing the thermodynamic phase diagram, we utilize the structures and energy data from the Materials Project Database [46]. The phase diagram construction is performed by methods implemented in PYMATGEN [47,48].

The electrochemical stability is estimated using a grand potential phase diagram method proposed by Ong *et al.* [47]. The interfaces of SSE with the anode and cathode are treated as open systems for diffusing ions, with $\mu_{\text{ion}} = \mu_{\text{ion}}^0$ at the anode and $\mu_{\text{ion}} = \mu_{\text{ion}}^0 - e\Delta V$ at the cathode, where μ_{ion}^0 is the chemical potential of the bulk alkali metal, e denotes the elementary charge, and ΔV is the voltage of the charged cathode relative to A/A^+ . The thermodynamic potential of a given phase that effected by applied voltage is expressed as $\phi = E - \mu_{\text{ion}}N_{\text{ion}}$, where E is the DFT energy and N_{ion} is the number of ions in that phase. The

phase equilibria at different voltages are then examined by phase diagram construction with ϕ [47,49,50].

Ab initio molecular dynamics (AIMD) simulations are performed in the NVT ensemble on the system containing 132 atoms, using the Nosé-Hoover thermostat for temperature control. For computational tractability, we employ a plane-wave energy cutoff of 400 eV and a Γ -centered $1 \times 1 \times 1$ k -point grid, in agreement with established methodologies by Ong *et al.* [51]. A time step of 2 fs is employed throughout the simulations. The simulation protocol initiates with structures assigned an initial temperature of 300 K following a Boltzmann distribution. Subsequently, the system temperature is increased to the target range (500–1400 K) through velocity scaling during the initial 2 ps (1000 time steps), followed by a 10 ps (5000 time steps) equilibration process under NVT conditions. The molecular dynamics (MD) simulations for diffusion are then performed for 100–500 ps. Throughout the AIMD simulations, all systems maintain structural integrity without observable degradation. The diffusion coefficients (D) are calculated through the Einstein relation:

$$D = \frac{\text{MSD}(\Delta t)}{2d\Delta t}, \quad (1)$$

where d represents the dimension of diffusion, MSD denotes the mean squared displacement and Δt is the time interval. The MSD is calculated as

$$\text{MSD}(\Delta t) = \frac{1}{N} \sum_{i=1}^N |\mathbf{r}_i(\Delta t) - \mathbf{r}_i(0)|^2, \quad (2)$$

where N is total number of diffusion ions, and r_i represents the position vector of the i th ion. For enhanced statistical accuracy in first-principles MD simulations, we employ the running-window method for MSD calculation [52]:

$$\text{MSD}(\Delta t) = \frac{1}{N} \sum_{i=1}^N \frac{1}{N_{\Delta t}} \sum_{t=0}^{t_{\text{tot}}-\Delta t} |\mathbf{r}_i(t + \Delta t) - \mathbf{r}_i(t)|^2 \quad (3)$$

this approach yields more reliable diffusion properties by averaging over multiple time origins. When performing linear fitting for diffusion coefficient determination, both the initial ballistic regime and the late-stage nonlinear deviations caused by insufficient statistical sampling

are systematically excluded. The ionic conductivity (σ) is calculated by the Nernst-Einstein relation:

$$\sigma = \frac{N}{V} \frac{q^2}{k_B T} D, \quad (4)$$

where N is the number of mobile ions, V is the volume of the simulation cell, q is the charge of the ion, k_B is the Boltzmann constant, and T is the temperature. The room-temperature conductivity ($\sigma_{300\text{K}}$) and activation energy (E_a) are determined from Arrhenius plots:

$$\sigma T = \sigma_0 \exp\left(-\frac{E_a}{k_B T}\right), \quad (5)$$

where σ_0 is the pre-exponential factor, E_a is the activation energy.

Transition state migration energy barriers are calculated using the climbing image nudged elastic band (CI-NEB) method available in VTST [53,54], with six and eight images inserted based on the length of diffusion path. The forces are converged to within 0.05 eV/Å.

C. Machine-learning models

First-principles calculations are limited to systems containing several hundred atoms, making it challenging to achieve a fully converged dynamical description for superionic conductors [55–57]. To overcome this limitation, we combine machine-learning models with molecular dynamics simulations to study ion dynamics for $M_5\text{YSi}_4\text{O}_{12}$ ($M = \text{Li}, \text{Na}, \text{K}$). The machine-learning potentials (MLPs) are developed using the Attention Coupled Neural Network (ACNN) package [58]. The training set is created by selecting every fifth structure from the AIMD trajectory, while the test set is formed by choosing every 20th structure from the remaining pool, resulting in datasets containing 393 136, 308 929, and 530 332 structures for $\text{Li}_5\text{YSi}_4\text{O}_{12}$, $\text{Na}_5\text{YSi}_4\text{O}_{12}$, and $\text{K}_5\text{YSi}_4\text{O}_{12}$, respectively. We use Chebyshev polynomial expansions up to the 12th order for radial basis functions within a 8.0 Å cutoff and up to the 10th order for angular functions within a 8.0 Å cutoff. The MLPs are trained for 2 000 000 backpropagation (BP) steps with an initial learning rate of 0.001 that is adjusted every 8000 steps using a decay factor of 0.95. The model parameters are saved every 20 000 steps. The final potential achieved energy errors below 1 meV/atom and force errors below 100 meV/Å on both training and test sets. Detailed accuracy tests are presented in Figs. S6–S8.

Since the training set and validation dataset are derived from identical trajectories, raising potential overfitting concerns, we rigorously validate the machine-learning potentials through an independent procedure. Specifically, we perform separate 500 ps AIMD simulations to construct independent validation sets containing 10 000 configurations for $M_5\text{YSi}_4\text{O}_{12}$ ($M = \text{Li}, \text{Na}, \text{K}$). As demonstrated

in Fig. S12, the evaluation results from models saved at 20 000-step intervals during training reveal that all three MLPs consistently achieve stable performance plateaus in the later stages, with no observable signs of overfitting.

MLPs are integrated into the LAMMPS package [59] to perform large-scale molecular dynamics simulations. MLP-accelerated molecular dynamics (MLP-MD) employs the Nosé-Hoover thermostat to maintain isothermal conditions within the temperature range of 600–1000 K. The time step is set to 2 fs, consistent with the AIMD simulations. Five distinct system sizes are simulated for each compound, spanning from $1 \times 1 \times 1$ (132 atoms) to $10 \times 10 \times 10$ (132 000 atoms) to systematically examine finite-size effects. Each temperature-cell size combination is sampled with five independent trajectories generated using different initial velocity distributions, ensuring statistical robustness. All simulations achieve thermodynamic equilibrium before data collection. The simulation durations range from 100 ps to 2 ns, which we adjust based on convergence behavior. The MSD plots for $M_5\text{YSi}_4\text{O}_{12}$ ($M = \text{Li}, \text{Na}, \text{K}$) are presented in Figs. S14 and S15.

Diffusion coefficients are calculated for each temperature and cell size, with error bars representing the standard deviation across five replicate simulations. These uncertainties are incorporated as weights during linear regression of the Arrhenius plots [52]. Unlike the running-window method employed in AIMD, the MSD analysis for MLP-MD adopts a fixed-reference approach [Eq. (2)] due to the prohibitive computational cost of window averaging with large datasets. During linear fitting of diffusion coefficients, only the central 90% of the MSD data (5–95% range) is considered.

The NVT ensemble simulations are constrained to constant volume conditions, inherently exclude thermal expansion effects. To systematically assess the influence of thermal expansion on calculated ionic conductivity values across the studied temperature range, we perform additional simulations for $\text{K}_5\text{YSi}_4\text{O}_{12}$. We first equilibrate $\text{K}_5\text{YSi}_4\text{O}_{12}$ under the NPT ensemble for 5 ps across 600–1000 K to obtain thermally expanded structures. MLP-MD simulations are then conducted under NVT ensemble conditions for an $8 \times 8 \times 8$ supercell of $\text{K}_5\text{YSi}_4\text{O}_{12}$, with five independent simulations of 200 ps duration at each temperature point. Comparative analysis is subsequently performed between these results and those obtained from conventional NVT ensemble simulations of the $8 \times 8 \times 8$ supercell.

The potential training is performed using an NVIDIA RTX 4090 GPU with 24 GB memory, while molecular dynamics simulations are conducted on compute nodes equipped with AMD EPYC 7452 processors (48 cores) and 192 GB RAM. Benchmark tests reveal that for the $1 \times 1 \times 1$ supercell of $\text{Na}_5\text{YSi}_4\text{O}_{12}$, a 10 ps molecular dynamics simulation requires 16 h when using first-principles methods, whereas the MLP accomplishes the same task

in merely 25 s, achieving a 2300-fold acceleration in computational efficiency.

III. RESULTS AND DISCUSSION

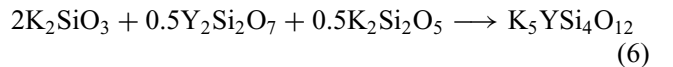
A. Thermodynamic and electrochemical stability

In Fig. 1, we present the structure of $M_5\text{YSi}_4\text{O}_{12}$, which features a corner-sharing network of YO_6 octahedra and SiO_4 tetrahedra. Twelve SiO_4 tetrahedra form $\text{Si}_{12}\text{O}_{36}$ rings that stack along the c -axis to create columns. Within the columns, 48 of the 90 M^+ ions per $M_{90}\text{Y}_{18}\text{Si}_{72}\text{O}_{216}$ unit cell occupy the $36f$ (M1), $6b$ (M2), and $6a$ (M3) Wyckoff positions. The columns are interconnected by YO_6 octahedra, creating large open channels between them. In these channels, the $36f$ positions (M5, M6) are partially occupied, whereas the $18e$ positions (M4) serve as connecting links between the channels. M4, M5, and M6 together account for the remaining 42 M^+ ions. The detailed crystallographic data of hexagonal $\text{Na}_5\text{YSi}_4\text{O}_{12}$ is provided in Table S1.

The lattice changes after substitution of sodium ions with lithium and potassium ions in $\text{Na}_5\text{YSi}_4\text{O}_{12}$ are listed in Table I. Substituting sodium ions in the structure causes lattice contraction for $\text{Li}_5\text{YSi}_4\text{O}_{12}$ and expansion for $\text{K}_5\text{YSi}_4\text{O}_{12}$, which is consistent with the ionic radius order of Li^+ , Na^+ , and K^+ [44]. The length of c -axis reflects the size of the open channels within the framework. Variations in the c -axis length suggest that the open

channel length decreases in the order of $\text{Li}_5\text{YSi}_4\text{O}_{12} < \text{Na}_5\text{YSi}_4\text{O}_{12} < \text{K}_5\text{YSi}_4\text{O}_{12}$. These changes in $M_5\text{YSi}_4\text{O}_{12}$ imply adjustments in the available space for ion diffusion, suggesting different diffusion patterns for Li, Na, and K ions in the structural framework.

We investigate the phase stability of $\text{Li}_5\text{YSi}_4\text{O}_{12}$ and $\text{K}_5\text{YSi}_4\text{O}_{12}$ by constructing the quaternary Li-Y-Si-O and K-Y-Si-O phase diagrams using all known Li-Y-Si-O and K-Y-Si-O compounds in the Material Project database. As shown in Fig. 2(a), $\text{Li}_5\text{YSi}_4\text{O}_{12}$ is identified as a metastable phase with an E_{hull} of 40 meV/atom. Despite its metastable nature, $\text{Li}_5\text{YSi}_4\text{O}_{12}$ has been successfully synthesized by Shannon *et al.* [7]. In Fig. 2(d), $\text{K}_5\text{YSi}_4\text{O}_{12}$ exhibits an E_{hull} of 0 eV, indicating its thermodynamic stability and potential for synthesis. Shannon *et al.* were unable to synthesize $\text{K}_5\text{YSi}_4\text{O}_{12}$ via the molten salt exchange method, likely due to the large ionic radius of potassium, which renders this approach ineffective. This suggests that alternative synthesis routes should be considered. Based on the K-Y-Si-O phase diagram, we calculated all possible synthesis pathways for $\text{K}_5\text{YSi}_4\text{O}_{12}$, as listed in Table S6. The pathway with the lowest energy change, which can avoid any side products, is



The calculated reaction energy for Eq. (6) is -0.74 eV. We provide the X-ray diffraction (XRD) patterns for $\text{K}_5\text{YSi}_4\text{O}_{12}$ in Fig. S4 to facilitate the verification of synthesis results.

Low electronic conductivity is crucial for solid electrolytes to prevent internal short circuits in batteries. As shown in Figs. 2(b) and 2(e) and Fig. S3(a), all three compounds exhibit wide band gaps: 4.52 eV for $\text{Li}_5\text{YSi}_4\text{O}_{12}$, 3.97 eV for $\text{Na}_5\text{YSi}_4\text{O}_{12}$, and 4.13 eV for $\text{K}_5\text{YSi}_4\text{O}_{12}$. These values clearly demonstrate their electrically insulating nature. We assess the electrochemical stability of $M_5\text{YSi}_4\text{O}_{12}$ using the grand potential approach [47,60, 61]. Figures 2(c) and 2(f) and Fig. S3(b) show the predicted phase equilibria at the interfaces between the solid electrolyte and both the metal anode and charged cathode. $\text{Li}_5\text{YSi}_4\text{O}_{12}$ is stable against Li uptake and loss within the voltage range of 1.26–3.72 V [Fig. 2(c)]. However, it is chemically vulnerable to phase instability at the voltage window and may decompose into $\text{Li}_2\text{Si}_2\text{O}_5$, Li_2SiO_3 , and $\text{Y}_2\text{Si}_2\text{O}_7$, indicating its low electrochemical stability. $\text{Na}_5\text{YSi}_4\text{O}_{12}$ demonstrates a wide experimental voltage window of up to 8 V [18]. Our calculation, however, reveals that $\text{Na}_5\text{YSi}_4\text{O}_{12}$ exhibits intrinsic electrochemical stability within a narrower range of 0.49–3.23 V [Fig. S3(b)]. It is not thermodynamically stable against sodium metal and is predicted to be reduced into NaYSiO_4 , Na_2SiO_3 and Si. Notably, both NaYSiO_4 and Na_2SiO_3 are electrically insulating, which could serve

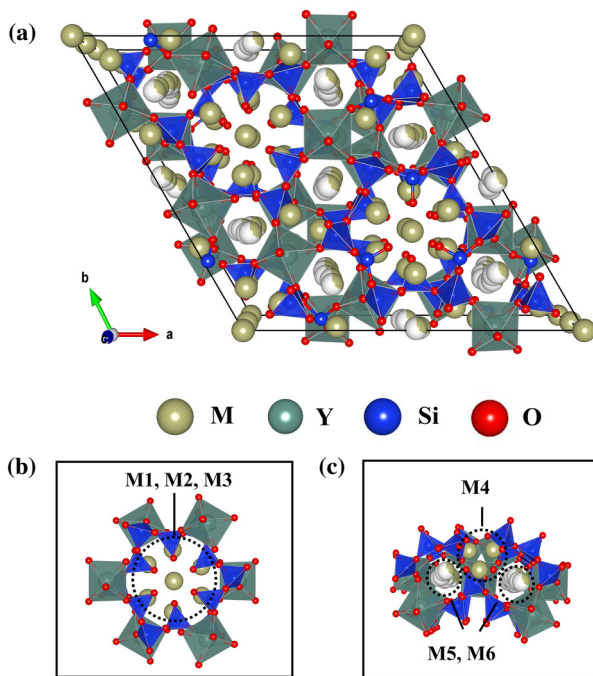


FIG. 1. (a) Crystal structure of $M_5\text{YSi}_4\text{O}_{12}$. (b) The $\text{Si}_{12}\text{O}_{36}$ ring formed by 12 SiO_4 tetrahedra. (c) Open channels interconnected by the M4 position.

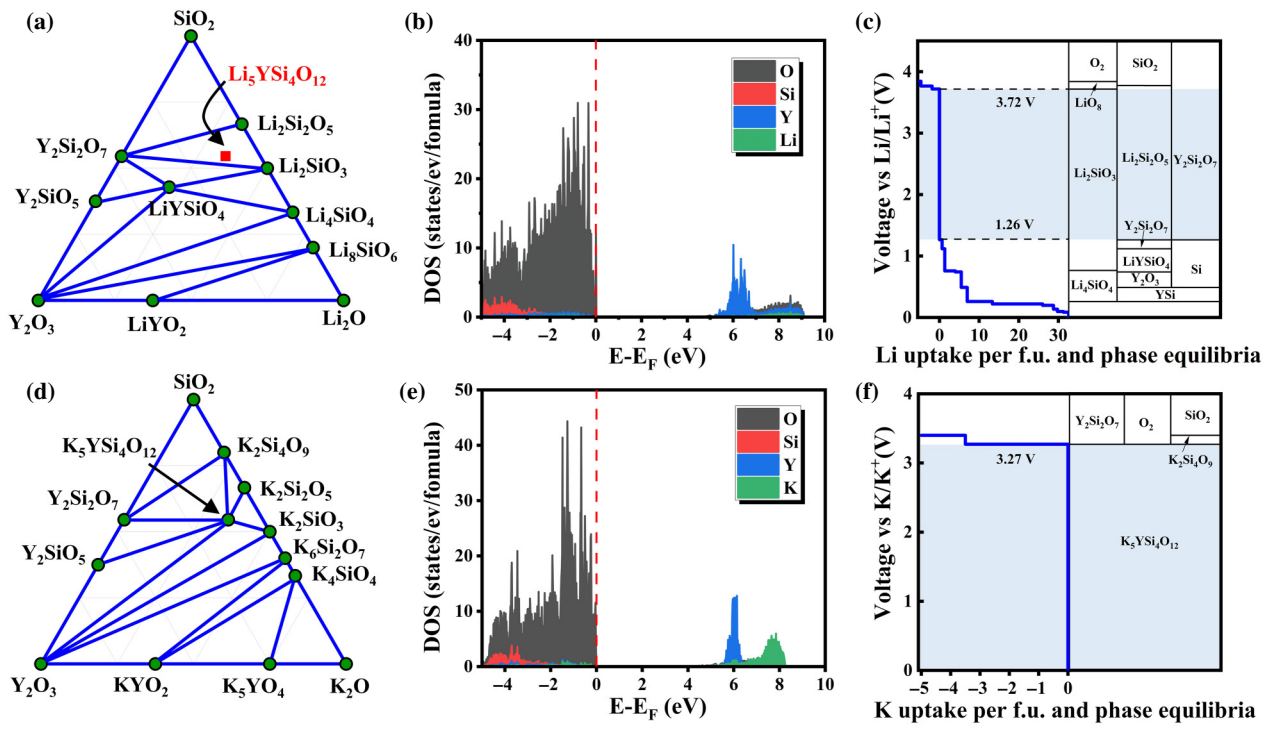


FIG. 2. Pseudoternary phase diagram of (a) Y_2O_3 - SiO_2 - Li_2O for $\text{Li}_5\text{YSi}_4\text{O}_{12}$ and (d) Y_2O_3 - SiO_2 - K_2O for $\text{K}_5\text{YSi}_4\text{O}_{12}$, where blue circles with labeled compositions represent stable phases, and red squares denote metastable phases with $E_{\text{hull}} > 0$. Density of states for (b) $\text{Li}_5\text{YSi}_4\text{O}_{12}$ and (e) $\text{K}_5\text{YSi}_4\text{O}_{12}$, and voltage window for (c) $\text{Li}_5\text{YSi}_4\text{O}_{12}$ and (f) $\text{K}_5\text{YSi}_4\text{O}_{12}$. The shaded squares represent the electrochemical stability window. Results for $\text{Na}_5\text{YSi}_4\text{O}_{12}$ are presented in Fig. S3.

as passivating interfacial layers between the electrolyte and electrode, thus extending the electrochemical stability window. $\text{K}_5\text{YSi}_4\text{O}_{12}$ exhibits a wide stability window [Fig. 2(f)]. The oxidation decomposition of $\text{K}_5\text{YSi}_4\text{O}_{12}$ occurs above 3.27 V to form $\text{Y}_2\text{Si}_2\text{O}_7$, $\text{K}_2\text{Si}_4\text{O}_9$, and O_2 . Notably, it is thermodynamically stable against potassium metal. Compatibility with metal anodes is essential for SSEs [61,62], as it prevents detrimental side reactions at the anode-SSE interface, thus enhancing the stability and rate performance of the whole battery. This is one of the core challenges faced by current SSEs [63]. With its intrinsic stability with potassium metal, $\text{K}_5\text{YSi}_4\text{O}_{12}$ is capable of minimizing the interfacial reactions.

B. Ionic conductivity

AIMD simulations are conducted at multiple temperatures for $M_5\text{YSi}_4\text{O}_{12}$ ($M = \text{Li}, \text{Na}, \text{K}$) to evaluate room-temperature ionic conductivity (σ_{RT}) and clarify the diffusion patterns of cations. As shown in Fig. 3(a), $\text{K}_5\text{YSi}_4\text{O}_{12}$ displays a smooth curve with a shallower slope, indicating a lower activation energy compared to $\text{Li}_5\text{YSi}_4\text{O}_{12}$ and $\text{Na}_5\text{YSi}_4\text{O}_{12}$. Detailed σ_{RT} and activation energies derived from AIMD simulations are presented in Table S7. The activation energies E_a are 273 meV for $\text{Li}_5\text{YSi}_4\text{O}_{12}$ and 198 meV for $\text{Na}_5\text{YSi}_4\text{O}_{12}$, with

extrapolated σ_{RT} of 0.66 and 4.81 mS/cm, respectively. The results for $\text{Na}_5\text{YSi}_4\text{O}_{12}$ align well with the experimental data from Sun *et al.* [18], who reported an activation barrier of 0.20 eV and a σ_{RT} of 1.59 mS/cm for $\text{Na}_5\text{YSi}_4\text{O}_{12}$. However, AIMD simulations for $\text{K}_5\text{YSi}_4\text{O}_{12}$ produced unexpectedly high ionic conductivity estimates. The extrapolated σ_{RT} reached 140.54 mS/cm with a low activation barrier of 72 meV, which greatly exceeds the typical value for SSEs, generally below 10 mS/cm [64]. We repeat five individual simulations at 300 K directly for $\text{K}_5\text{YSi}_4\text{O}_{12}$. As shown in Fig. S5, they yielded ionic conductivities ranging from 36 to 221 mS/cm. The abnormally high values observed for $\text{K}_5\text{YSi}_4\text{O}_{12}$ raise concerns about the reliability of results obtained from small simulation cells in AIMD. To validate our results, we expanded calculations using large simulation cells containing thousands to tens of thousands of atoms, which exceed the capabilities of AIMD and conducted by machine-learning-accelerated molecular dynamics.

Three individual MLPs are trained for $M_5\text{YSi}_4\text{O}_{12}$ ($M = \text{Li}, \text{Na}, \text{K}$) using the ACNN package. Figure 4 shows the comparison of radial distribution functions (RDFs) obtained from the MLP-MD and AIMD simulations. Detailed RDFs for all interatomic pairs are presented in Figs. S9–S11. The results of MLP-MD agree well with those from AIMD simulations for all three compounds,

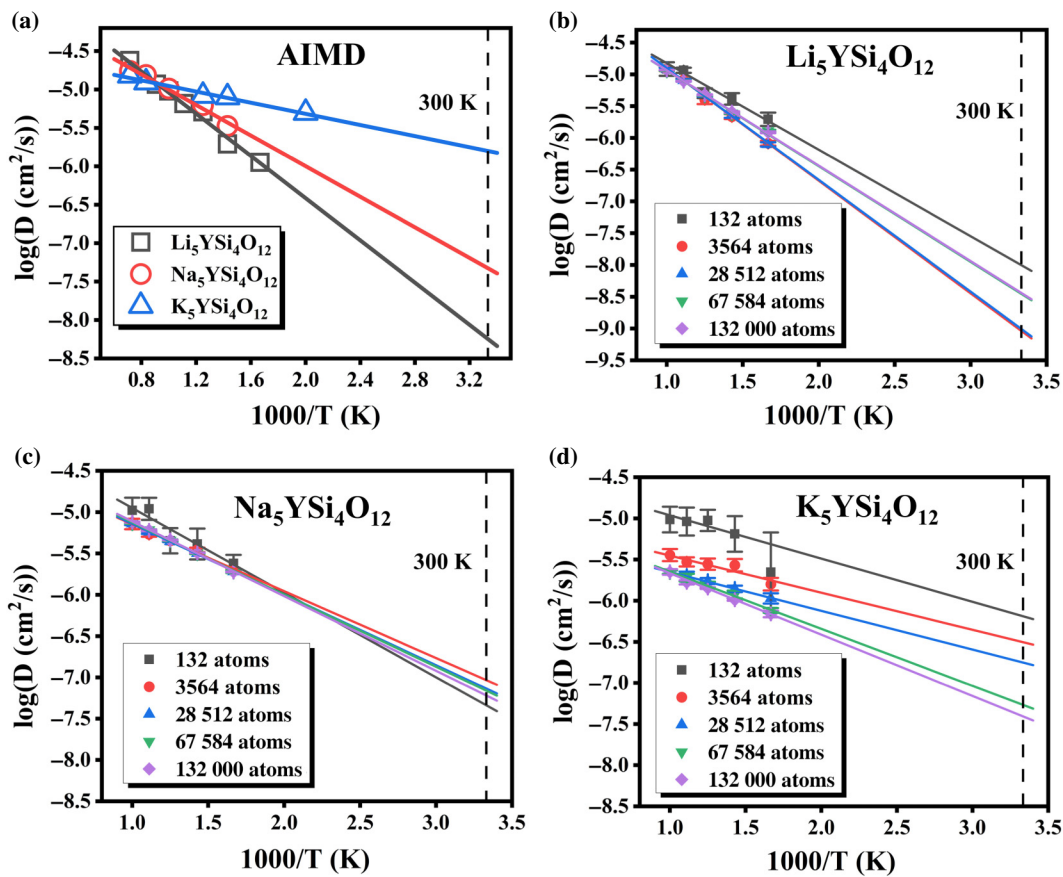


FIG. 3. (a) Arrhenius plot of ionic diffusivity for $M_5\text{YSi}_4\text{O}_{12}$ ($M = \text{Li}, \text{Na}, \text{K}$), calculated from AIMD simulations using 132-atom cells. (b)–(d) Arrhenius plots obtained from MLP-MD simulations for $\text{Li}_5\text{YSi}_4\text{O}_{12}$, $\text{Na}_5\text{YSi}_4\text{O}_{12}$, and $\text{K}_5\text{YSi}_4\text{O}_{12}$, respectively, across different simulation cell sizes.

indicating that the MLP-MD reproduced the structural properties in a statistical perspective. We perform MLP-MD for $M_5\text{YSi}_4\text{O}_{12}$ ($M = \text{Li}, \text{Na}, \text{K}$) using supercells ranging from $1 \times 1 \times 1$ (132 atoms) to $10 \times 10 \times 10$ (132 000 atoms) and at temperatures ranging from 600 to 1000 K. For each temperature, five individual simulations are conducted with distinct initial velocity seeds, resulting in a

total of 125 trajectories for each compound, as detailed in the Sec. II. Arrhenius plots of diffusivities for each supercell are shown in Figs. 3(b)–3(d). The derived σ_{RT} and activation energies for each supercell are presented in Table S7.

The variation of σ_{RT} with the size of supercell is illustrated in Fig. S13. MLP-MD for $\text{Li}_5\text{YSi}_4\text{O}_{12}$ and

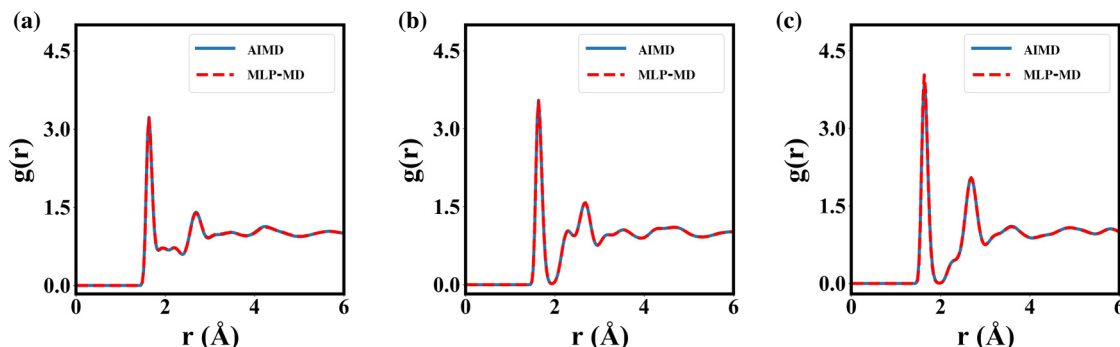


FIG. 4. Comparison of RDF of the entire structure between MLP-MD and AIMD at 1000 K for (a) $\text{Li}_5\text{YSi}_4\text{O}_{12}$, (b) $\text{Na}_5\text{YSi}_4\text{O}_{12}$, and (c) $\text{K}_5\text{YSi}_4\text{O}_{12}$. Comparison of all interatomic pairs are shown in Figs. S9–S11.

$\text{Na}_5\text{YSi}_4\text{O}_{12}$ show consistent σ_{RT} across different supercell sizes, in agreement with first-principles calculations. The calculated σ_{RT} from a $10 \times 10 \times 10$ supercell (132 000 atoms) for $\text{Li}_5\text{YSi}_4\text{O}_{12}$ and $\text{Na}_5\text{YSi}_4\text{O}_{12}$ is 0.43 and 6.11 mS/cm, respectively. The ionic conductivity calculated for $\text{Na}_5\text{YSi}_4\text{O}_{12}$ is consistent with the upper bound of single-crystal conductivity established experimentally by Beyeler *et al.* [8]. These results further verify the reliability of machine-learning-accelerated molecular dynamics that we adopt. However, $\text{K}_5\text{YSi}_4\text{O}_{12}$ demonstrates a clear decrease in σ_{RT} with increasing simulation cell size. MLP-MD calculated σ_{RT} for the $1 \times 1 \times 1$ (132 atoms) cell is 57.41 mS/cm, a notably high value for typical SSEs, similar to the results observed in AIMD. As the simulation cell size increases, σ_{RT} steadily decreases, eventually converging to 3.63 mS/cm in the largest cell containing 132 000 atoms. This value compares favorably with various potassium-based SSEs currently available, as summarized in Table S8. Coupled with the high electrochemical stability, $\text{K}_5\text{YSi}_4\text{O}_{12}$ is particularly well-suited for use in potassium-based ASSBs.

To examine whether the observed size-dependent ionic conductivity arises from thermostat-induced artifacts, we design two complementary simulation protocols, as detailed in Sec. VI.D of the Supplemental Material [33]. First, we employ the Langevin thermostat with two distinct damping parameters (100 and 1000 ps^{-1}) to examine systems of varying sizes (3564, 28 512, and 67 584 atoms). The resulting conductivity values (Table S9) and Arrhenius plots (Fig. S16) consistently demonstrate pronounced size effects regardless of damping parameters. Specifically, for the 100 ps^{-1} damping parameter, the conductivity drops from 12.53 to 1.34 mS cm^{-1} as the system size increases from 3564 to 67 584 atoms; similarly, at 1000 ps^{-1} , it decreases from 83.52 to 5.69 mS cm^{-1} . Second, to completely exclude thermostat influence, we perform combined NVT-NVE simulations on the 3564- and 67 584-atom systems. Each simulation consists of NVT equilibration and production employing the Nosé-Hoover thermostat, followed by NVE production where the thermostat is removed. As shown in Fig. S17 and Table S10, the consistent MSD curves and temperature stability confirm that removing the thermostat does not alter system dynamics. Furthermore, Fig. S18 and Table S11 reveal that ionic conductivity exhibits size dependence in both ensembles. For the simulation using NVE ensemble without thermostat, the conductivity decreases from 25.01 mS/cm (3564 atoms) to 4.60 mS/cm (67 584 atoms). These results demonstrate that the choice of thermostat does not affect the observed size effects in $\text{K}_5\text{YSi}_4\text{O}_{12}$.

Another potential factor influencing ionic conductivity is the contribution from ballistic regimes. To evaluate the effect of ballistic regimes, we perform comparative analyses for the 3564- and 67 584-atom systems over a fixed 200 ps simulation duration, as detailed in Sec. VI.E of the

Supplemental Material [33]. Following the methodology of He *et al.* [52], we identify the ballistic regimes by examining the MSD curves at 1000 K. As shown in Fig. S19, the ballistic regime extends up to 3 ps for the 3564-atom system and 6 ps for the 67 584-atom system, beyond which the MSD-time curves become linear. These early time ballistic regions have been systematically excluded by fitting the central portion of MSD data in our calculations, where the minimum time origin is set at 10 ps for $\text{K}_5\text{YSi}_4\text{O}_{12}$, thereby minimizing their influence on the calculated diffusion coefficients. As shown in Fig. S20 and Table S12, the 67 584-atom system consistently yield lower ionic conductivity than the 3564-atom system under identical analysis time windows, reproducing the observed size effects. These analyses confirms that the size dependence of ionic conductivity does not originate from ballistic contributions.

The effect of thermal expansion on ionic conductivity in $\text{K}_5\text{YSi}_4\text{O}_{12}$ is also evaluated. As presented in Table S13, the system volume increases with temperature, reaching a maximum expansion of 4.59% at 1000 K. The expansion leads to enhanced diffusion coefficients (Fig. S21). However, the room-temperature ionic conductivity only slightly decreases from 4.79 mS/cm (NVT ensemble) to 4.36 mS/cm (Table S14). This minor difference arises from the increased activation barrier induced by thermal expansion, suggesting a negligible effect on the overall conductivity predictions.

We further investigate the effect of simulation duration for systems with identical sizes. As detailed in Sec. VI.G of the Supplemental Material [33], we monitor the evolution of diffusion coefficients with simulation time for $1 \times 1 \times 1$, $6 \times 6 \times 6$, and $8 \times 8 \times 8$ supercells at 1000 K. The results demonstrate that extended simulation time ensures convergence for all three systems. More importantly, increasing the supercell size not only accelerates convergence but also substantially reduces the error bars in final results.

C. Diffusion patterns

Clarifying the atomistic diffusion mechanisms in SSEs is essential for gaining deep insights into their structure framework. We calculate the probability density function from AIMD simulations for $M_5\text{YSi}_4\text{O}_{12}$ ($M = \text{Li}, \text{Na}, \text{K}$) at 800 K, with identified diffusion pathways presented in Fig. 5. The atomic trajectories obtained from 100 ps AIMD simulations at 1000 K are presented in Fig. S23, which provides direct visualization of the ionic diffusion mode variations [65]. CI-NEB calculations are performed to calculate the vacancy migration barriers in the identified pathways. The corresponding calculated CI-NEB migration barriers are given in Fig. 6 for $\text{Li}_5\text{YSi}_4\text{O}_{12}$ and $\text{K}_5\text{YSi}_4\text{O}_{12}$. The migration barriers for $\text{Na}_5\text{YSi}_4\text{O}_{12}$ calculated by Sun *et al.* [18] are adopted for comparison.

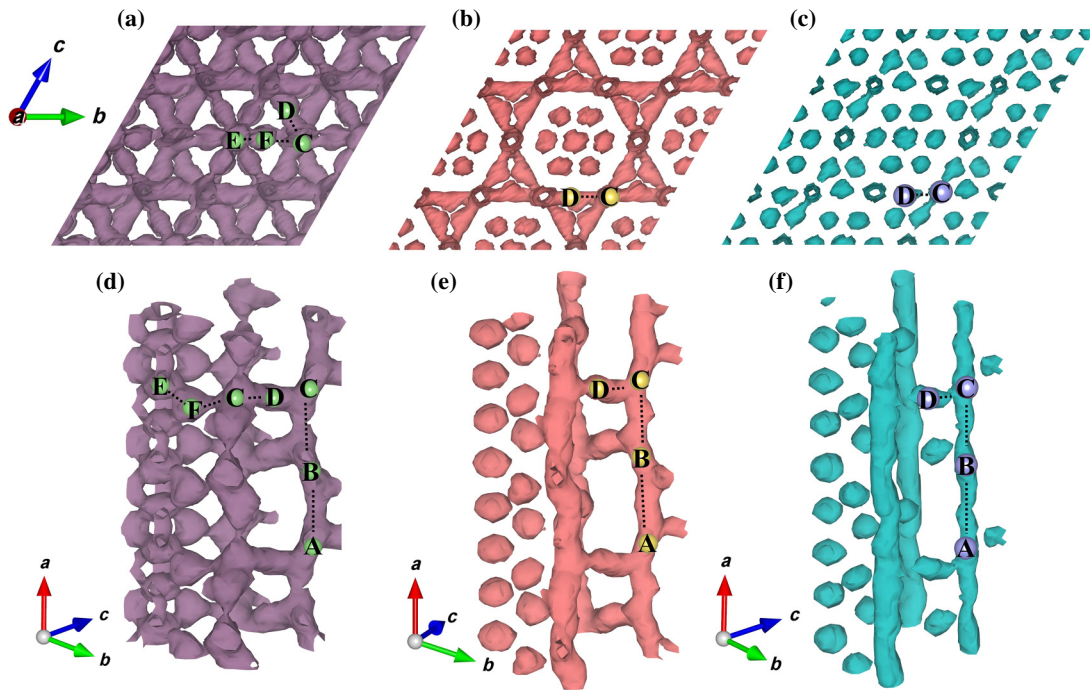


FIG. 5. Probability density plots for: (a),(d) Li^+ in $\text{Li}_5\text{YSi}_4\text{O}_{12}$; (b),(e) Na^+ in $\text{Na}_5\text{YSi}_4\text{O}_{12}$; and (c),(f) K^+ in $\text{K}_5\text{YSi}_4\text{O}_{12}$. Isosurfaces of the probability densities are plotted at isovalues $P_0/4$, in which P_0 is defined as the mean value of the density. Letters and dashed lines are used to show the diffusion pathways.

As shown in Figs. 5(b) and 5(e) and Fig. S23(b,e), two distinct behaviors of sodium ions are identified in $\text{Na}_5\text{YSi}_4\text{O}_{12}$. Sodium ions within the columns [Fig. 1(b)] only vibrate around equilibrium positions, showing a restricted, near-circular probability density. The other sodium ions at M4, M5, and M6 sites exhibit an extended

probability density. They diffuse along the open channels created by interconnected columns and hop between channels via the M4 site. These results are in agreement with the hypothesis proposed by Beyeler *et al.* [8] and the results by Sun *et al.* [18]. The energy barriers for the two migration pathways ($\text{A} \rightarrow \text{B} \rightarrow \text{C}$ and $\text{C} \rightarrow \text{D}$) calculated by Sun *et al.* [18] reveals that the energy barrier for ion movement within the channels is 0.72 eV, significantly higher than the 0.26 eV required for diffusion in the plane along $\text{C} \rightarrow \text{D}$. This suggests that Na^+ diffusion in $\text{Na}_5\text{YSi}_4\text{O}_{12}$ occurs more readily within the ab plane than along the open channels. However, as shown in Figs. 5(b) and 5(e), the overall Na^+ migration through the lattice requires movement along the channels. This suggests that the relatively high migration barrier within the channels serves as the primary limiting factor for achieving higher ionic conductivity in $\text{Na}_5\text{YSi}_4\text{O}_{12}$.

For $\text{Li}_5\text{YSi}_4\text{O}_{12}$, all lithium ions participate in the diffusion process, including those sites within the columns, forming a three-dimensional diffusion network. As shown in Figs. 5(a) and 5(d) and Fig. S23(a,d), two additional diffusion pathways ($\text{E} \rightarrow \text{F}$ and $\text{F} \rightarrow \text{C}$) connect the ions within the columns to the sites located between the columns. Figures 6(a) and 6(b) presents the energy barriers for the diffusion pathways within $\text{Li}_5\text{YSi}_4\text{O}_{12}$. The energy barrier for the diffusion pathways along the channel ($\text{A} \rightarrow \text{B} \rightarrow \text{C}$) is as high as 1303 meV, significantly higher than that of the in-plane pathways ($\text{E} \rightarrow \text{F} \rightarrow \text{C} \rightarrow \text{D}$)

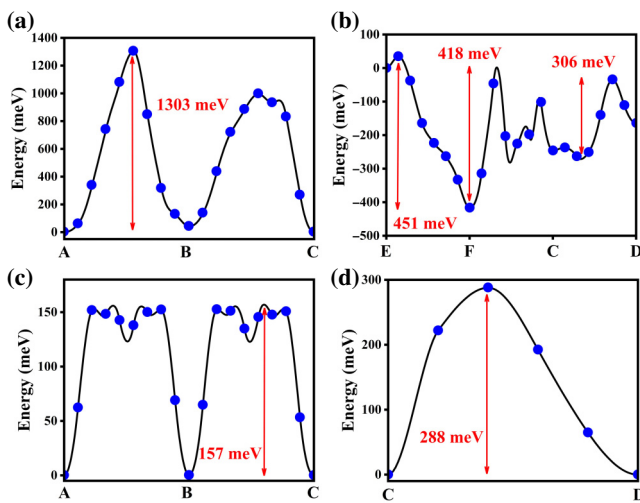


FIG. 6. (a),(b) Energy barriers for vacancy migration in $\text{Li}_5\text{YSi}_4\text{O}_{12}$: (a) along the open channel and (b) in the plane. (c),(d) Energy barriers for vacancy migration in $\text{K}_5\text{YSi}_4\text{O}_{12}$: (c) along the open channel and (d) in the plane.

calculated at 418 meV. This indicates that lithium primarily diffuses within the plane rather than along the channels, which is similar to $\text{Na}_5\text{YSi}_4\text{O}_{12}$. Notably, the migration barriers for lithium ions along equivalent pathways in $\text{Li}_5\text{YSi}_4\text{O}_{12}$ are higher than those in $\text{Na}_5\text{YSi}_4\text{O}_{12}$ (0.72 eV in-plane and 0.26 eV along the open channels), suggesting that lithium ion mobility is more restricted. Besides, the newly identified pathways in $\text{Li}_5\text{YSi}_4\text{O}_{12}$ ($\text{E} \rightarrow \text{F} \rightarrow \text{C}$) exhibit relatively high migration barriers of 418 meV compared with the $\text{C} \rightarrow \text{D}$ pathway (306 meV). As a result, these new pathways may have limited effectiveness in enhancing the ionic conductivity.

The diffusion behavior of potassium ions in $\text{K}_5\text{YSi}_4\text{O}_{12}$ is distinct compared with that of lithium and sodium ions in $\text{Li}_5\text{YSi}_4\text{O}_{12}$ and $\text{Na}_5\text{YSi}_4\text{O}_{12}$. As shown in Figs. 5(c) and 5(f) and Fig. S23(c,f), the probability density of $\text{K}_5\text{YSi}_4\text{O}_{12}$ is predominantly concentrated within the open channels, with a notably lower density in the regions between channels compared to $\text{Na}_5\text{YSi}_4\text{O}_{12}$. No probability density is observed within the columns. This suggests that potassium ions primarily diffuse within the open channels. Diffusion between channels through $\text{C} \rightarrow \text{D}$ is suppressed for potassium ions. This can be explained by the results of migration barriers. As shown in Figs. 6(c) and 6(d), the migration energy barrier for potassium ions along the open channel is 157 meV, significantly lower than the 288 meV barrier in the plane. The difference in energy barriers between these pathways leads to the preferential diffusion of potassium ions along the open channels than in the plane, in contrast to $\text{Li}_5\text{YSi}_4\text{O}_{12}$ and $\text{Na}_5\text{YSi}_4\text{O}_{12}$.

We calculate the directional diffusion coefficients following the methodology established by Mo *et al.* [65], with detailed computational procedures provided in Sec. VII.B of the Supplemental Material [33]. As shown in Fig. S24 and Table S15, $\text{Li}_5\text{YSi}_4\text{O}_{12}$ exhibits higher ionic conductivity perpendicular to the channels (0.58 mS/cm) than along them (0.22 mS/cm). $\text{Na}_5\text{YSi}_4\text{O}_{12}$ shows high conductivity in both directions, indicating three-dimensional isotropic diffusion. For $\text{K}_5\text{YSi}_4\text{O}_{12}$, as shown in Fig. S25 and Table S16, our simulations reveal that the conductivity along the channels is significantly higher than that perpendicular to the channels, clearly demonstrating one-dimensional diffusion characteristics along the channel.

The differences in diffusion patterns of $M_5\text{YSi}_4\text{O}_{12}$ ($M = \text{Li}, \text{Na}, \text{K}$) are attributed to variations in the ionic radii of M ions. A smaller ionic radius promotes the formation of diffusion pathways that are less suitable for larger ions. Consequently, lithium in $\text{Li}_5\text{YSi}_4\text{O}_{12}$ exhibits the richest diffusion behavior, followed by sodium in $\text{Na}_5\text{YSi}_4\text{O}_{12}$, whereas potassium, with its largest ionic radius, displays the most restricted diffusion patterns. However, despite lithium exhibiting the most extensive diffusion patterns, $\text{Li}_5\text{YSi}_4\text{O}_{12}$ exhibits the lowest ionic conductivity among $M_5\text{YSi}_4\text{O}_{12}$ ($M = \text{Li}, \text{Na}, \text{K}$). This can

be attributed to two factors. First, the small volume of $\text{Li}_5\text{YSi}_4\text{O}_{12}$ limits the hopping distance of individual diffusion events, whereas the large volume of $\text{K}_5\text{YSi}_4\text{O}_{12}$ facilitates enhanced ionic conductivity. As recently proposed by López *et al.* [66], fast diffusion of ions in SSEs is strongly correlated with ample hopping lengths, rather than high hopping frequencies. We calculate the average diffusing distance at multiple temperatures for $M_5\text{YSi}_4\text{O}_{12}$ ($M = \text{Li}, \text{Na}, \text{K}$). As presented in Table S17–S19, potassium ions achieve the longest diffusion distances, nearly twice those of lithium and sodium across various temperatures. This suggests that the diffusion events in $\text{K}_5\text{YSi}_4\text{O}_{12}$ are more effective than in $\text{Li}_5\text{YSi}_4\text{O}_{12}$. Second, the high energy barriers in the diffusion pathways of $\text{Li}_5\text{YSi}_4\text{O}_{12}$ hinder ion diffusion in $\text{Li}_5\text{YSi}_4\text{O}_{12}$, particularly at low temperatures. The high energy barrier causes a steeper slope in the Arrhenius plot and a rapid decrease in diffusion coefficients as the temperature drops. Consequently, although all lithium ions are capable of diffusing within the structural framework, the room-temperature ionic conductivity of $\text{Li}_5\text{YSi}_4\text{O}_{12}$ remains low. In contrast, $\text{K}_5\text{YSi}_4\text{O}_{12}$ benefits from a combination of low migration barriers and long hopping distances, resulting in high room-temperature ionic conductivity.

D. Size effect

The calculated σ_{RT} of $\text{K}_5\text{YSi}_4\text{O}_{12}$ exhibits a significant size effect, with the estimated values decrease as the simulation cell size increases. Convergence is achieved only when employing a sufficiently large simulation supercell. Previous studies have examined the effect of simulation size on diffusivity, which can be broadly classified into three key aspects. First, diffusion processes that occur in larger cells may not be fully captured in smaller ones. For instance, Ceder *et al.* [67] demonstrated that point defects in LiFePO_4 are undervalued at nanoscale. These point defects would restrict the diffusion of lithium ions as particle size increases, resulting in a scale-dependent intrinsic diffusion coefficients. Second, the application of periodic boundary conditions in simulations of bulk materials introduces interactions between atoms in the simulation box and their periodic images, affecting dynamical properties and leading to size effect [68]. Yeh and Hummer [69] demonstrate that, due to the long-range nature of hydrodynamic interactions, diffusion coefficients significantly increase with larger system sizes in simulations of water and Lennard-Jones fluids. Third, traditional AIMD simulations are typically restricted to systems containing only a few hundred atoms and subnanosecond timescales. These limitations hinder the exploration of a sufficient number of diffusion events [52,56,57], thus compromising the convergence of diffusion coefficients and leading to overestimated values. For example, Huang *et al.* [55] conducted a convergence test on the diffusion coefficients

of $\text{Li}_{10}\text{GeP}_2\text{S}_{12}$. Their results showed that convergence improved with increasing simulation time and cell size, as more diffusion events were captured. By analyzing the convergence and number of diffusion events in our simulations of $\text{K}_5\text{YSi}_4\text{O}_{12}$, we conclude that the size effect observed in $\text{K}_5\text{YSi}_4\text{O}_{12}$ arises primarily from limited convergence in smaller simulation cells as proposed by Huang *et al.* [55]. This effect is especially pronounced at low temperatures, where the slow dynamics of ions make it more challenging to capture the diffusion events.

Figure 7(a) presents the error bars for $\log(D)$ (where D represents the diffusion coefficients and $\log(D)$ is employed to enhance clarity in the presentation of the data) of $\text{K}_5\text{YSi}_4\text{O}_{12}$ at various temperatures and cell sizes. The results indicate that the error bars for diffusivity decrease as the simulation cell size increases, demonstrating improved convergence with larger supercells. In addition, at a fixed cell size, the error bar of $\log(D)$ exhibits a decreasing trend with increasing temperature. This behavior can be attributed to the faster ionic dynamics at high temperatures. We also calculated the number of diffuse events for

$M_5\text{YSi}_4\text{O}_{12}$ ($M = \text{Li}, \text{Na}, \text{K}$) using the approach described by He *et al.* [52], which involves dividing the total mean squared displacement by a^2 , where a is the single hopping distance provided in Tables S17–S19. Figure 7(b) compares the number of diffusion events at 1000 K. Among the three compounds, potassium exhibits the fewest diffusion events, significantly lower than lithium and sodium. The diffusion events show a decreasing trend and converge with increasing cell size. This indicates the pronounced size effect observed in $\text{K}_5\text{YSi}_4\text{O}_{12}$ is caused by limited diffusion events at small supercells that hinder the convergence, which is not as evident in $\text{Li}_5\text{YSi}_4\text{O}_{12}$ or $\text{Na}_5\text{YSi}_4\text{O}_{12}$. Similar trends are observed at 800 and 900 K, as illustrated in Fig. S26. The observed size effects in $\text{K}_5\text{YSi}_4\text{O}_{12}$ highlight the importance of testing for convergence in diffusivity simulations of superionic conductors. Such assessments are crucial to ensure reliable and accurate simulation outcomes.

IV. CONCLUSIONS

In summary, we have investigated the stability and ionic conductivity of the $M_5\text{YSi}_4\text{O}_{12}$ family ($M = \text{Li}, \text{K}$). Our study confirms that $\text{Li}_5\text{YSi}_4\text{O}_{12}$ is thermodynamically unstable, with an energy above the convex hull of 40 meV/atom, whereas $\text{K}_5\text{YSi}_4\text{O}_{12}$ is thermodynamically stable, showing potential for synthesis. Both compounds are insulators with wide band gaps. Notably, $\text{K}_5\text{YSi}_4\text{O}_{12}$ demonstrates a broad electrochemical stability window starting at 0 V vs. K/K^+ , suggesting its compatibility with potassium metal anode and its ability to minimize interfacial reactions. In contrast, $\text{Li}_5\text{YSi}_4\text{O}_{12}$ demonstrates low electrochemical stability, with complex side reactions occurring at the interfaces between the SSEs and both the anode and charged cathode. To evaluate their ionic conductivities, AIMD simulations and machine-learning-accelerated molecular dynamics have been employed. The σ_{RT} values are determined to be 0.43 and 3.63 mS/cm for $\text{Li}_5\text{YSi}_4\text{O}_{12}$ and $\text{K}_5\text{YSi}_4\text{O}_{12}$, respectively, using a $10 \times 10 \times 10$ (132 000 atoms) simulation cell. In addition, simulations on $\text{K}_5\text{YSi}_4\text{O}_{12}$ reveal a significant size effect, where the estimated ionic conductivity decreases as the cell size increases. This behavior is attributed to fewer diffusion events in smaller cells, resulting in limited convergence and an overestimation of σ_{RT} . In conclusion, our findings highlight $\text{K}_5\text{YSi}_4\text{O}_{12}$ as a promising SSE for K-ion batteries and underscore the importance of scale in the modeling of ionic conductivity.

ACKNOWLEDGMENTS

This work is supported by the National Key R&D Program of China (Grant No. 2023YFB3003001), the National Natural Science Foundation of China (Grant Nos. 12374008 and 12022408), the Interdisciplinary Integration and Innovation Project of JLU, and Fundamental Research

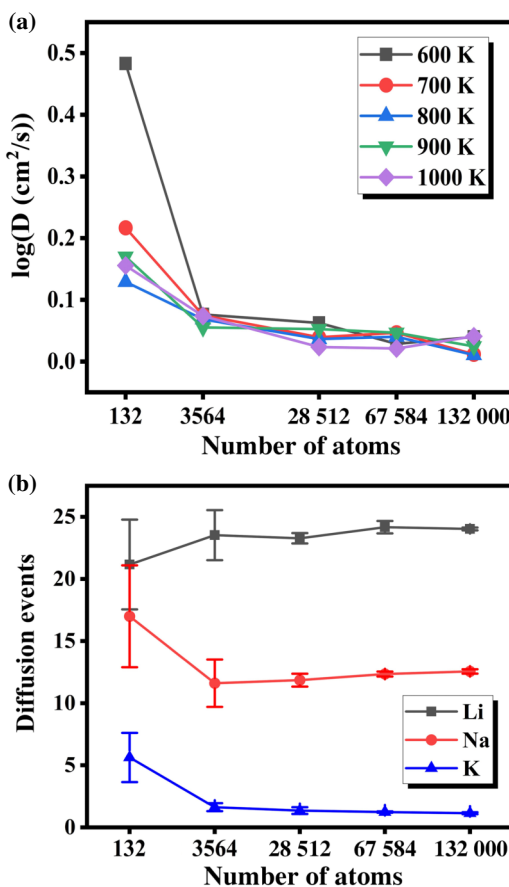


FIG. 7. (a) Variation of the error bars for $\log(D)$ at different temperatures with increasing simulation cell size for $\text{K}_5\text{YSi}_4\text{O}_{12}$. (b) Variation of diffusion events per 132 atoms per 10 ps with simulation cell size for $M_5\text{YSi}_4\text{O}_{12}$ at 1000 K.

Funds for the Central Universities and the Program for JLU Science and Technology Innovative Research Team (JLUSTIRT).

DATA AVAILABILITY

The data that support the findings of this article are not publicly available upon publication because it is not technically feasible and/or the cost of preparing, depositing, and hosting the data would be prohibitive within the terms of this research project. The data are available from the authors upon reasonable request.

- [1] Y.-K. Sun, Promising all-solid-state batteries for future electric vehicles, *ACS Energy Lett.* **5**, 3221 (2020).
- [2] A. M. Bates, Y. Preger, L. Torres-Castro, K. L. Harrison, S. J. Harris, and J. Hewson, Are solid-state batteries safer than lithium-ion batteries? *Joule* **6**, 742 (2022).
- [3] J. G. Kim, B. Son, S. Mukherjee, N. Schuppert, A. Bates, O. Kwon, M. J. Choi, H. Y. Chung, and S. Park, A review of lithium and non-lithium based solid state batteries, *J. Power Sources* **282**, 299 (2015).
- [4] H.-D. Lim, J.-H. Park, H.-J. Shin, J. Jeong, J. T. Kim, K.-W. Nam, H.-G. Jung, and K. Y. Chung, A review of challenges and issues concerning interfaces for all-solid-state batteries, *Energy Storage Mater.* **25**, 224 (2020).
- [5] G. Liu, J. Yang, J. Wu, Z. Peng, and X. Yao, Inorganic sodium solid electrolytes: Structure design, interface engineering and application, *Adv. Mater.* **36**, 2311475 (2024).
- [6] H. Yang and N. Wu, Ionic conductivity and ion transport mechanisms of solid-state lithium-ion battery electrolytes: A review, *Energy Sci. Eng.* **10**, 1643 (2022).
- [7] R. D. Shannon, B. E. Taylor, T. E. Gier, H. Y. Chen, and T. Berzins, Ionic conductivity in sodium yttrium silicon oxide ($\text{Na}_5\text{YSi}_4\text{O}_{12}$)-type silicates, *Inorg. Chem.* **17**, 958 (1978).
- [8] H. U. Beyeler, R. D. Shannon, and H. Y. Chen, Ionic conductivity of single-crystal $\text{Na}_5\text{YSi}_4\text{O}_{12}$, *Appl. Phys. Lett.* **37**, 934 (1980).
- [9] K. Yamashita, New fast sodium-ion conducting glass-ceramics of silicophosphates: Crystallization, microstructure and conduction properties, *Solid State Ionics* **35**, 299 (1989).
- [10] L.-I. Hung, S.-L. Wang, S.-P. Szu, C.-Y. Hsieh, H.-M. Kao, and K.-H. Lii, Hydrothermal synthesis, crystal structure, solid-state NMR spectroscopy, and ionic conductivity of $\text{Na}_5\text{InSi}_4\text{O}_{12}$, a silicate containing a single 12-membered ring, *Chem. Mater.* **16**, 1660 (2004).
- [11] T. Okura, N. Yoshida, and K. Yamashita, Na^+ superionic conducting silicophosphate glass-ceramics—Review, *Solid State Ionics* **285**, 143 (2016).
- [12] J. Schilm, R. Anton, D. Wagner, J. Huettl, M. Kusnezoff, M. Herrmann, H. K. Kim, and C. W. Lee, Influence of $R = \text{Y}, \text{Gd}, \text{Sm}$ on crystallization and sodium ion conductivity of $\text{Na}_5\text{RSi}_4\text{O}_{12}$ phase, *Materials* **15**, 1104 (2022).
- [13] H.-B. Sun, J.-Z. Guo, Y. Zhang, T. Wei, Y.-X. Zhou, L.-L. Zhang, X.-L. Wu, Y. Huang, and W. Luo, High-voltage all-solid-state Na-ion-based full cells enabled by all

NASICON-structured materials, *ACS Appl. Mater. Interfaces* **11**, 24192 (2019).

- [14] J. Hüttl, W. Cai, D. Wagner, J. Schilm, M. Kusnezoff, K. Nikolowski, N. Shaji, C. Lee, M. Partsch, and A. Michaelis, Polarization impedance at the $\text{Na}-\text{Na}_5\text{YSi}_4\text{O}_{12}$ interface, *Solid State Ionics* **376**, 115856 (2022).
- [15] G. Sun, C. Lou, B. Yi, W. Jia, Z. Wei, S. Yao, Z. Lu, G. Chen, Z. Shen, M. Tang, and F. Du, Electrochemically induced crystalline-to-amorphization transformation in sodium samarium silicate solid electrolyte for long-lasting sodium metal batteries, *Nat. Commun.* **14**, 6501 (2023).
- [16] A. Yang, K. Yao, M. Schaller, E. Dashjav, H. Li, S. Zhao, Q. Zhang, M. Etter, X. Shen, H. Song, Q. Lu, R. Ye, I. Moudrakovski, Q. Pang, S. Indris, X. Wang, Q. Ma, F. Tietz, J. Chen, and O. Guillou, Enhanced room-temperature Na^+ ionic conductivity in $\text{Na}_{4.92}\text{Y}_{0.92}\text{Zr}_{0.08}\text{Si}_4\text{O}_{12}$, *eScience* **3**, 100175 (2023).
- [17] A. Michalak, S. Behara, and A. R. M. Reinvestigation of $\text{Na}_5\text{GdSi}_4\text{O}_{12}$: A potentially better solid electrolyte than sodium β alumina for solid-state sodium batteries, *ACS Appl. Mater. Interfaces* **16**, 7112 (2024).
- [18] G. Sun, X. Yang, N. Chen, S. Yao, X. Wang, X. Jin, G. Chen, Y. Xie, and F. Du, $\text{Na}_5\text{YSi}_4\text{O}_{12}$: A sodium superionic conductor for ultrastable quasi-solid-state sodium-ion batteries, *Energy Storage Mater.* **41**, 196 (2021).
- [19] J. Huang, K. Wu, G. Xu, M. Wu, S. Dou, and C. Wu, Recent progress and strategic perspectives of inorganic solid electrolytes: Fundamentals, modifications, and applications in sodium metal batteries, *Chem. Soc. Rev.* **52**, 4933 (2023).
- [20] A. Hayashi, K. Noi, A. Sakuda, and M. Tatsumisago, Superionic glass-ceramic electrolytes for room-temperature rechargeable sodium batteries, *Nat. Commun.* **3**, 856 (2012).
- [21] C. Lou, J. Liu, X. Sun, W. Zhang, L. Xu, H. Luo, Y. Chen, X. Gao, X. Kuang, J. Fu, J. Xu, L. Su, J. Ma, and M. Tang, Correlating local structure and migration dynamics in Na/Li dual ion conductor $\text{Na}_5\text{YSi}_4\text{O}_{12}$, *Proc. Natl. Acad. Sci.* **121**, e2401109121 (2024).
- [22] A. Haffner, A.-K. Hatz, O. E. O. Zeman, C. Hoch, B. V. Lotsch, and D. Johrendt, Polymorphism and fast potassium-ion conduction in the T5 supertetrahedral phosphidosilicate KSi_2P_3 , *Angew. Chem. Int. Ed.* **60**, 13641 (2021).
- [23] M. Zhou, P. Bai, X. Ji, J. Yang, C. Wang, and Y. Xu, Electrolytes and interphases in potassium ion batteries, *Adv. Mater.* **33**, 2003741 (2021).
- [24] S. Ferrari, M. Falco, A. B. Muñoz-García, M. Bonomo, S. Brutti, M. Pavone, and C. Gerbaldi, Solid-state post Li metal ion batteries: A sustainable forthcoming reality? *Adv. Energy Mater.* **11**, 2100785 (2021).
- [25] Y. Xu, Y. Du, H. Chen, J. Chen, T. Ding, D. Sun, D. H. Kim, Z. Lin, and X. Zhou, Recent advances in rational design for high-performance potassium-ion batteries, *Chem. Soc. Rev.* **53**, 7202 (2024).
- [26] J.-Y. Hwang, S.-T. Myung, and Y.-K. Sun, Recent progress in rechargeable potassium batteries, *Adv. Funct. Mater.* **28**, 1802938 (2018).
- [27] W. Zhang, J. Yin, W. Wang, Z. Bayhan, and H. N. Alshareef, Status of rechargeable potassium batteries, *Nano Energy* **83**, 105792 (2021).

- [28] J. Shao, J. Zheng, L. Qin, S. Zhang, Y. Ren, and Y. Wu, K₃SbS₄ as a potassium superionic conductor with low activation energy for K–S batteries, *Angew. Chem. Int. Ed.* **61**, e202200606 (2022).
- [29] H. Wang, Y. Chen, Z. D. Hood, G. Sahu, A. S. Pandian, J. K. Keum, K. An, and C. Liang, An air-stable Na₃SbS₄ superionic conductor prepared by a rapid and economic synthetic procedure, *Angew. Chem. Int. Ed.* **55**, 8551 (2016).
- [30] J. C. Bachman, S. Muy, A. Grimaud, H.-H. Chang, N. Pour, S. F. Lux, O. Paschos, F. Maglia, S. Lupart, P. Lamp, L. Giordano, and Y. Shao-Horn, Inorganic solid-state electrolytes for lithium batteries: Mechanisms and properties governing ion conduction, *Chem. Rev.* **116**, 140 (2016).
- [31] W. D. Richards, T. Tsujimura, L. J. Miara, Y. Wang, J. C. Kim, S. P. Ong, I. Uechi, N. Suzuki, and G. Ceder, Design and synthesis of the superionic conductor Na₁₀SnP₂S₁₂, *Nat. Commun.* **7**, 11009 (2016).
- [32] X. Bai, Y. Duan, W. Zhuang, R. Yang, and J. Wang, Research progress in Li-argyrodite-based solid-state electrolytes, *J. Mater. Chem. A* **8**, 25663 (2020).
- [33] See Supplemental Material at <https://link.aps.org/supplemental/10.1103/8wkh-238p> for: detailed structure information of M₅YSi₄O₁₂; the electrochemical stability of Na₅YSi₄O₁₂; accuracy of machine-learning models; potential synthesis routes for K₅YSi₄O₁₂; MSD plots for M₅YSi₄O₁₂; results of Langevin thermostat simulations; discussion of thermal expansion effects; large-scale molecular dynamics results; direction-dependent ionic conductivities; and average diffusion distances for M₅YSi₄O₁₂. The Supplemental Material also contains Refs. [35–43].
- [34] S. P. Ong, W. D. Richards, A. Jain, G. Hautier, M. Kocher, S. Cholia, D. Gunter, V. L. Chevrier, K. A. Persson, and G. Ceder, Python materials genomics (pymatgen): A robust, open-source python library for materials analysis, *Comput. Mater. Sci.* **68**, 314 (2013).
- [35] S. Yi, W. Zhou, Z. Wang, M. Yang, J.-F. Wu, and J. Liu, Layered K₂Mg₂TeO₆ solid electrolyte enables long-life solid-state potassium batteries, *ACS Energy Lett.* **9**, 2626 (2024).
- [36] X. Zhang, B. Yi, W. Jia, S. Zhao, S. Savilov, S. Yao, Z. X. Shen, G. Chen, Z. Wei, and F. Du, Boosting K⁺–ionic conductivity of layered oxides via regulating P2/P3 heterogeneity and reciprocity for room-temperature quasi-solid-state potassium metal batteries, *Angew. Chem. Int. Ed.* **64**, e202413214 (2025).
- [37] R. Zhang, S. Xu, L. Wang, C. Wang, Y. Zhou, Z. Lü, W. Li, D. Xu, S. Wang, and X. Yang, Theoretical study on ion diffusion mechanism in W-doped K₃SbS₄ as solid-state electrolyte for K-ion batteries, *Inorg. Chem.* **63**, 6743 (2024).
- [38] C. Kim, J. Park, H. Kwak, J.-S. Kim, S. Jun, D.-H. Seo, and Y. S. Jung, KTaCl₆: High-voltage stable potassium-ion conducting chloride solid electrolyte, *Energy Storage Mater.* **71**, 103618 (2024).
- [39] Y. Zhang, P. Qiu, J. Zheng, X. Chen, X.-M. Chen, S. Li, C. Ji, Y. Wu, and X. Chen, KB₃H₈ · NH₃B₃H₇ complex as a potential solid-state electrolyte with excellent stability against K metal, *ACS Appl. Mater. Interfaces* **14**, 17378 (2022).
- [40] X. Lu, M. E. Bowden, V. L. Sprenkle, and J. Liu, A low cost, high energy density, and long cycle life potassium–sulfur battery for grid-scale energy storage, *Adv. Mater.* **27**, 5915 (2015).
- [41] J. Zheng, H. Fang, L. Fan, Y. Ren, P. Jena, and Y. Wu, Antiperovskite K₃ OI for K-ion solid state electrolyte, *J. Phys. Chem. Lett.* **12**, 7120 (2021).
- [42] Y. Chen, P. Wang, E. Truong, B. Ogbolu, Y. Jin, I. Oyekunle, H. Liu, M. M. Islam, T. Poudel, C. Huang, I. Hung, Z. Gan, and Y.-Y. Hu, Superionic conduction in K₃SbS₄ enabled by Cl-modified anion lattice, *Angew. Chem. Int. Ed.* **63**, e202408574 (2024).
- [43] J. Shao, H. Ao, L. Qin, J. Elgin, C. E. Moore, Y. Khalifa, S. Zhang, and Y. Wu, Design and synthesis of cubic K_{3–2x}Ba_xSbSe₄ solid electrolytes for K–O₂ batteries, *Adv. Mater.* **35**, 2306809 (2023).
- [44] R. D. Shannon, Revised effective ionic radii and systematic studies of interatomic distances in halides and chalcogenides, *Acta Crystallogr. Sect. A* **32**, 751 (1976).
- [45] G. Kresse and J. Furthmüller, Efficient iterative schemes for *ab initio* total-energy calculations using a plane-wave basis set, *Phys. Rev. B* **54**, 11169 (1996).
- [46] A. Jain, S. P. Ong, G. Hautier, W. Chen, W. D. Richards, S. Dacek, S. Cholia, D. Gunter, D. Skinner, G. Ceder, and K. A. Persson, Commentary: The Materials Project: A materials genome approach to accelerating materials innovation, *APL Mater.* **1**, 011002 (2013).
- [47] S. P. Ong, L. Wang, B. Kang, and G. Ceder, Li–Fe–P–O₂ phase diagram from first principles calculations, *Chem. Mater.* **20**, 1798 (2008).
- [48] A. Jain, G. Hautier, S. P. Ong, C. J. Moore, C. C. Fischer, K. A. Persson, and G. Ceder, Formation enthalpies by mixing GGA and GGA + *U* calculations, *Phys. Rev. B* **84**, 045115 (2011).
- [49] Z. Deng, Z. Zhu, I.-H. Chu, and S. P. Ong, Data-driven first-principles methods for the study and design of alkali superionic conductors, *Chem. Mater.* **29**, 281 (2017).
- [50] D. C. Lynch, Y. Li, P. Canepa, and N. A. W. Holzwarth, Computational investigation of the structural and electrolyte properties of the extended family of lithium (thio)boracite materials: Li₄B₇O₁₂Cl and beyond, *Phys. Rev. Mater.* **8**, 065401 (2024).
- [51] S. P. Ong, Y. Mo, W. D. Richards, L. Miara, H. S. Lee, and G. Ceder, Phase stability, electrochemical stability and ionic conductivity of the Li_{10±1}MP₂X₁₂ (*M* = Ge, Si, Sn, Al or P, and *X* = O, S or Se) family of superionic conductors, *Energy Environ. Sci.* **6**, 148 (2013).
- [52] X. He, Y. Zhu, A. Epstein, and Y. Mo, Statistical variances of diffusional properties from ab initio molecular dynamics simulations, *npj Comput. Mater.* **4**, 18 (2018).
- [53] G. Henkelman, B. P. Uberuaga, and H. Jónsson, A climbing image nudged elastic band method for finding saddle points and minimum energy paths, *J. Chem. Phys.* **113**, 9901 (2000).
- [54] G. Henkelman and H. Jónsson, Improved tangent estimate in the nudged elastic band method for finding minimum energy paths and saddle points, *J. Chem. Phys.* **113**, 9978 (2000).
- [55] J. Huang, L. Zhang, H. Wang, J. Zhao, J. Cheng, and W. E, Deep potential generation scheme and simulation protocol

- for the $\text{Li}_{10}\text{GeP}_2\text{S}_{12}$ -type superionic conductors, *J. Chem. Phys.* **154**, 094703 (2021).
- [56] J. Wang, A. A. Panchal, and P. Canepa, Strategies for fitting accurate machine-learned inter-atomic potentials for solid electrolytes, *Mater. Futures* **2**, 015101 (2023).
- [57] J. Qi, S. Banerjee, Y. Zuo, C. Chen, Z. Zhu, M. Holekevi Chandrappa, X. Li, and S. Ong, Bridging the gap between simulated and experimental ionic conductivities in lithium superionic conductors, *Mater. Today Phys.* **21**, 100463 (2021).
- [58] J. Li, J. Feng, J. Luo, B. Jiang, X. Zheng, J. Lv, K. Butler, H. Liu, C. Xie, Y. Xie, and Y. Ma, Enhancing the efficiency of complex systems crystal structure prediction by active learning guided machine learning potential, *ArXiv:2505.08159*.
- [59] A. P. Thompson, H. M. Aktulga, R. Berger, D. S. Bolintineanu, W. M. Brown, P. S. Crozier, P. J. In 'T Veld, A. Kohlmeyer, S. G. Moore, T. D. Nguyen, R. Shan, M. J. Stevens, J. Tranchida, C. Trott, and S. J. Plimpton, LAMMPS—A flexible simulation tool for particle-based materials modeling at the atomic, meso, and continuum scales, *Comput. Phys. Commun.* **271**, 108171 (2022).
- [60] S. P. Ong, A. Jain, G. Hautier, B. Kang, and G. Ceder, Thermal stabilities of delithiated olivine MPO_4 ($\text{M} = \text{Fe}, \text{Mn}$) cathodes investigated using first principles calculations, *Electrochim. Commun.* **12**, 427 (2010).
- [61] F. Han, Y. Zhu, X. He, Y. Mo, and C. Wang, Electrochemical stability of $\text{Li}_{10}\text{GeP}_2\text{S}_{12}$ and $\text{Li}_7\text{La}_3\text{Zr}_2\text{O}_{12}$ solid electrolytes, *Adv. Energy Mater.* **6**, 1501590 (2016).
- [62] Y. Zhu, X. He, and Y. Mo, Origin of outstanding stability in the lithium solid electrolyte materials: Insights from thermodynamic analyses based on first-principles calculations, *ACS Appl. Mater. Interfaces* **7**, 23685 (2015).
- [63] H. Adenusi, G. A. Chass, S. Passerini, K. V. Tian, and G. Chen, Lithium batteries and the solid electrolyte interphase (SEI)—Progress and outlook, *Adv. Energy Mater.* **13**, 2203307 (2023).
- [64] K. Jun, Y. Sun, Y. Xiao, Y. Zeng, R. Kim, H. Kim, L. J. Miara, D. Im, Y. Wang, and G. Ceder, Lithium superionic conductors with corner-sharing frameworks, *Nat. Mater.* **21**, 924 (2022).
- [65] Y. Mo, S. P. Ong, and G. Ceder, First principles study of the $\text{Li}_{10}\text{GeP}_2\text{S}_{12}$ lithium super ionic conductor material, *Chem. Mater.* **24**, 15 (2012).
- [66] C. López, R. Rurali, and C. Cazorla, How concerted are ionic hops in inorganic solid-state electrolytes? *J. Am. Chem. Soc.* **146**, 8269 (2024).
- [67] G. Ceder, R. Malik, D. Burch, and M. Bazant, 1D diffusion, *Nano Lett.* **10**, 4123 (2010).
- [68] A. T. Celebi, S. H. Jamali, A. Bardow, T. J. H. Vlugt, and O. A. Moulton, Finite-size effects of diffusion coefficients computed from molecular dynamics: A review of what we have learned so far, *Mol. Simul.* **47**, 831 (2021).
- [69] I.-C. Yeh and G. Hummer, System-size dependence of diffusion coefficients and viscosities from molecular dynamics simulations with periodic boundary conditions, *J. Phys. Chem. B* **108**, 15873 (2004).